EES Batteries

PAPER

View Article Online
View Journal | View Issue

Check for updates

Cite this: *EES Batteries*, 2025, **1**, 1693

Scalable upcycling of spent $LiNi_xCo_yMn_{1-x-y}O_2$ to single-crystal Ni-rich cathodes using a low-cost, multifunctional Ni salt

Xiaolu Yu,[a] Greta Feague,[b] Sicen Yu,[a] Varun Gupta,[a] Hongpeng Gao,[a] Wei Li,[b] Maura Appleberry,[b] Ping Liu, [a,b,c] Jiao Lin*[b] and Zheng Chen *[a,b,c]

The urgent need to recycle spent lithium-ion batteries (LIBs) is driven by the dual pressure of raw material scarcity and ecological sustainability. Closed-loop recycling of spent LIBs not only recovers valuable materials but also minimizes harmful environmental impact, offering an efficient strategy to meet the increasing demand for critical resources. Here, we introduce a thermally driven selective upcycling process that extracts lithium from spent polycrystalline $LiNi_{0.33}Co_{0.33}Mn_{0.33}O_2$ (NCM111) using $NiSO_4$. This process subsequently converts the residual materials into single-crystal Ni-rich cathodes with minimal input of nickel and lithium. We demonstrate that both chemically delithiated NCM111 and spent NCM111 black mass can be upgraded in terms of composition, structure, and electrochemical performance to match pristine $LiNi_{0.6}Co_{0.2}Mn_{0.2}O_2$ (NCM622) and $LiNi_{0.8}Co_{0.1}Mn_{0.1}O_2$ (NCM811). Life-cycle analysis reveals that this closed-loop selective upcycling approach significantly reduces energy consumption and greenhouse gas emissions, offering superior economic and environmental advantages over conventional hydrometallurgical, pyrometallurgical, and cathode production methods. This work establishes a foundation for cost-effective upcycling strategies, advancing the sustainable development of NCM materials and selective recovery for LIBs.

Received 7th July 2025,
Accepted 13th September 2025

DOI: 10.1039/d5eb00128e

rsc.li/EESBatteries

Open Access Article. Published on 15 September 2025. Downloaded on 12/24/2025 10:16:25 PM.
This article is licensed under a Creative Commons Attribution-NonCommercial 3.0 Unported Licence.

Broader context

The exponential rise in electric vehicles and grid-scale energy storage systems has intensified the demand for lithium-ion batteries (LIBs), bringing about mounting concerns regarding the sustainability of raw material supply and end-of-life (EoL) battery management. Traditional recycling methods such as pyrometallurgy and hydrometallurgy are resource-intensive and environmentally taxing, often resulting in elemental recovery rather than the regeneration of high-value cathode materials. Direct recycling has emerged as a more sustainable pathway but remains limited by structural degradation and feedstock variability. This study introduces a scalable, thermally driven selective upcycling strategy that transforms spent LIB cathodes into next-generation single-crystal Ni-rich materials with high electrochemical performance and phase purity. By utilizing a low-cost, multifunctional nickel salt for lithium extraction and compositional enhancement, the method eliminates harsh chemicals and minimizes energy use and greenhouse gas emissions. This work offers a pragmatic solution to close the loop in battery manufacturing and advances circular economy goals, positioning selective upcycling as a pivotal enabler for clean energy technologies.

1. Introduction

Over the past few decades, the surging demand for lithium-ion batteries (LIBs) has been driven by their widespread use in portable electronics, electric vehicles (EVs), and large-scale energy storage systems.[1–3] However, the disposal of end-of-life (EoL) LIBs poses a significant challenge to industry due to resource scarcity, ecological concerns, and environmental sustainability issues. To address this challenge, three main strategies for handing EoL LIBs have emerged, including downcycling, direct recycling, and upcycling. Downcycling methods, primarily hydrometallurgical and pyrometallurgical processes, are widely adopted in the industry.[4–6] These processes, however, involve high energy consumption and the use of harsh chemicals, such as high-temperature smelting, acid leaching, and chemical precipitation.[4,5,7,8] This results in considerable CO_2 emissions and hazardous waste generation, raising concerns about their long-term sustainability. In con-

[a]*Program of Materials Science and Engineering, University of California, San Diego, La Jolla, CA 92093, USA*
[b]*Aiiso Yufeng Li Family Department of Chemical and Nano Engineering, University of California, San Diego, La Jolla, CA 92093, USA. E-mail: zhc199@ucsd.edu, jil432@ucsd.edu*
[c]*Sustainable Power and Energy Center, University of California, San Diego, La Jolla, CA 92093, USA*

© 2025 The Author(s). Published by the Royal Society of Chemistry

Open Access Article. Published on 15 September 2025. Downloaded on 12/24/2025 10:16:25 PM.
This article is licensed under a Creative Commons Attribution-NonCommercial 3.0 Unported Licence.

trast, direct recycling retains the embedded energy and the cathode active material (CAM) structure, leading to lower energy consumption and reduced greenhouse gas emissions.[9,10] Despite these advantages, direct recycling faces challenges due to the complexity of material composition, variation of the crystal structure, and different degradation states of CAMs,[5,7,11–13] The need for tailored recycling approaches to handle a diverse range of impurities and degradation levels further complicates the process. For example, the physicochemical properties of recycled materials are often constrained by the degradation state of the original cathodes, limiting the potential for increasing nickel (Ni) content and addressing different spent cathodes.[14] All of these limitations hinder the successful scale-up of the direct recycling process.[15,16]

As the demand for high-energy density and low-cost cathode materials grows, downcycled and directly recycled products may no longer meet future performance requirements. Next-generation cathode materials, such as Ni-rich $LiNi_xCo_yMn_zO_2$ ($0 < x,y,z < 1$, $x + y + z = 1$, $x > 0.5$, NCM*xyz*), $LiMn_xFe_{1-x}PO_4$ (LMFP), and Li-rich Mn-based materials, are being developed to offer enhanced energy density.[9,17,18] Among these, single-crystal Ni-rich cathodes have gained increasing interest due to their superior structural stability, attributed to their smaller specific surface area and more uniform stress distribution compared to conventional polycrystalline particles.[19] This shift underscores the urgent need for advanced upcycling methods capable of meeting the demands of next-generation materials. Recent advancements have demonstrated the potential of upcycling methods, such as molten salt techniques, to upgrade lower-grade cathodes. For example, a LiOH-Li_2SO_4 salt mixture has been used to upgrade polycrystalline NCM111 and $LiNi_{0.5}Co_{0.3}Mn_{0.2}O_2$ (NCM532)[20] into single-crystal NCM622.[21] Other systems, such as a ternary molten salt system ($LiNO_3$–LiCl–NaOH), have been developed for upcycling spent NCM111 into $LiNi_{0.6}Co_{0.2}Mn_{0.2}O_2$ (NCM622).[22] However, these systems generate some unexpected pollutant gases, such as NO_2 and SO_2, which pose environmental risks. Our group previously reported an efficient method to upgrade polycrystalline delithiated NCM 111 (D-NCM 111) into single-crystal upcycled NCM622 (U-NCM622) and $LiNi_{0.8}Co_{0.1}Mn_{0.1}O_2$ (U-NCM811) using LiOH as the sole lithium source.[23] Nevertheless, challenges remain, particularly when dealing with low-nickel cathodes and varying feedstocks with different degradation levels.

In this work, we present an efficient upcycling method for upgrading degraded polycrystalline NCM111 into various single-crystal Ni-rich materials (*e.g.*, NCM 622 and NCM 811) by a rational design and selection of a multifunctional Ni salt precursor, which not only effectively extracts lithium from bulk crystals under mild roasting conditions without generating waste but also serves as the feedstock to enhance the Ni content in the upcycled product. Our approach involves spent battery-based, acid-free selective extraction of lithium from spent polycrystalline NCM111 and subsequent conversion of the remaining transition metal oxide (TMO) solids into various Ni-rich single-crystal particles with the desired Ni content. The versatility of this straightforward method is further validated through successful synthesis of NCM622 and NCM811 by adjusting precursor ratios and testing various batch sizes as well as by using spent cathode black mass feedstocks. The versatility of this method stems from its scalability and compositional flexibility, enabling the synthesis of different NCMs from diverse feedstocks through simple tuning of precursor ratios. Comprehensive materials characterization confirms the uniformity of Ni valence and its homogeneous distribution within the single-crystal particles. The upcycled Ni-rich cathodes exhibited significant enhancements in rate capability and cycling stability, outperforming their polycrystalline counterparts. This upcycling method offers substantial economic and environmental benefits by reducing energy consumption and greenhouse gas emissions, presenting a scalable and sustainable solution for LIB recycling.

2. Results and discussion

2.1 Selective upcycling process

An overview of the selective upcycling process is illustrated in Fig. 1a and Fig. S1, and it comprises two stages: selective lithium extraction and material upcycling.[24] In the first stage, D-NCM111 is ground and mixed with $NiSO_4$ in a specific molar ratio and then calcined in a muffle furnace at a mild temperature. $NiSO_4$ acts as a conversion agent, selectively extracting lithium from polycrystalline D-NCM111 while maintaining sulfur in the stable SO_4^{2-} form to generate Li_2SO_4. Since Li_2SO_4 is water-soluble, it is subsequently leached out using deionized water, leaving behind insoluble Ni–Co–Mn transition metal oxide (TMO) solids, which are readily separated by filtration to serve as the precursor for the next step of synthesis. The resulting Li_2SO_4 solution can be further purified and concentrated for recovery and reuse in lithium salt production as reported,[25] enhancing the sustainability of the process. In the second stage, the solid TMO feedstock is added with a balanced amount of nickel hydroxide ($Ni(OH)_2$) by ball milling to achieve the desired transition metal ratios for upcycling. This ball-milling process crushed D-NCM111 into its primary grains, which were then thoroughly mixed with LiOH in a 1 : 1.07 molar ratio. This mixture is sintered under oxygen to obtain single-crystal Ni-rich cathodes.

To gain insights into the conversion mechanisms during the selective upcycling process, scanning electron microscopy (SEM) imaging was used to observe the surface morphology. The SEM image of D-NCM111 in Fig. 1b consists of irregularly sized, rough spherical particles. $NiSO_4{\cdot}6H_2O$ appears as sharp-edged, rough square fragments (Fig. S2a). After mixing and grinding, both NCM111 and $NiSO_4$ are still recognizable according to their original morphology (Fig. S2b). After mild roasting, their original structures are indistinguishable (Fig. 1c). After the extraction of Li_2SO_4, the surface of the TMO precursor shows increased porosity (Fig. 1d). Interestingly, the TMO precursor partially retains the original spherical morphology of D-NCM111 (Fig. 1d), which can be attributed to the

© 2025 The Author(s). Published by the Royal Society of Chemistry

Open Access Article. Published on 15 September 2025. Downloaded on 12/24/2025 10:16:25 PM.
This article is licensed under a Creative Commons Attribution-NonCommercial 3.0 Unported Licence.

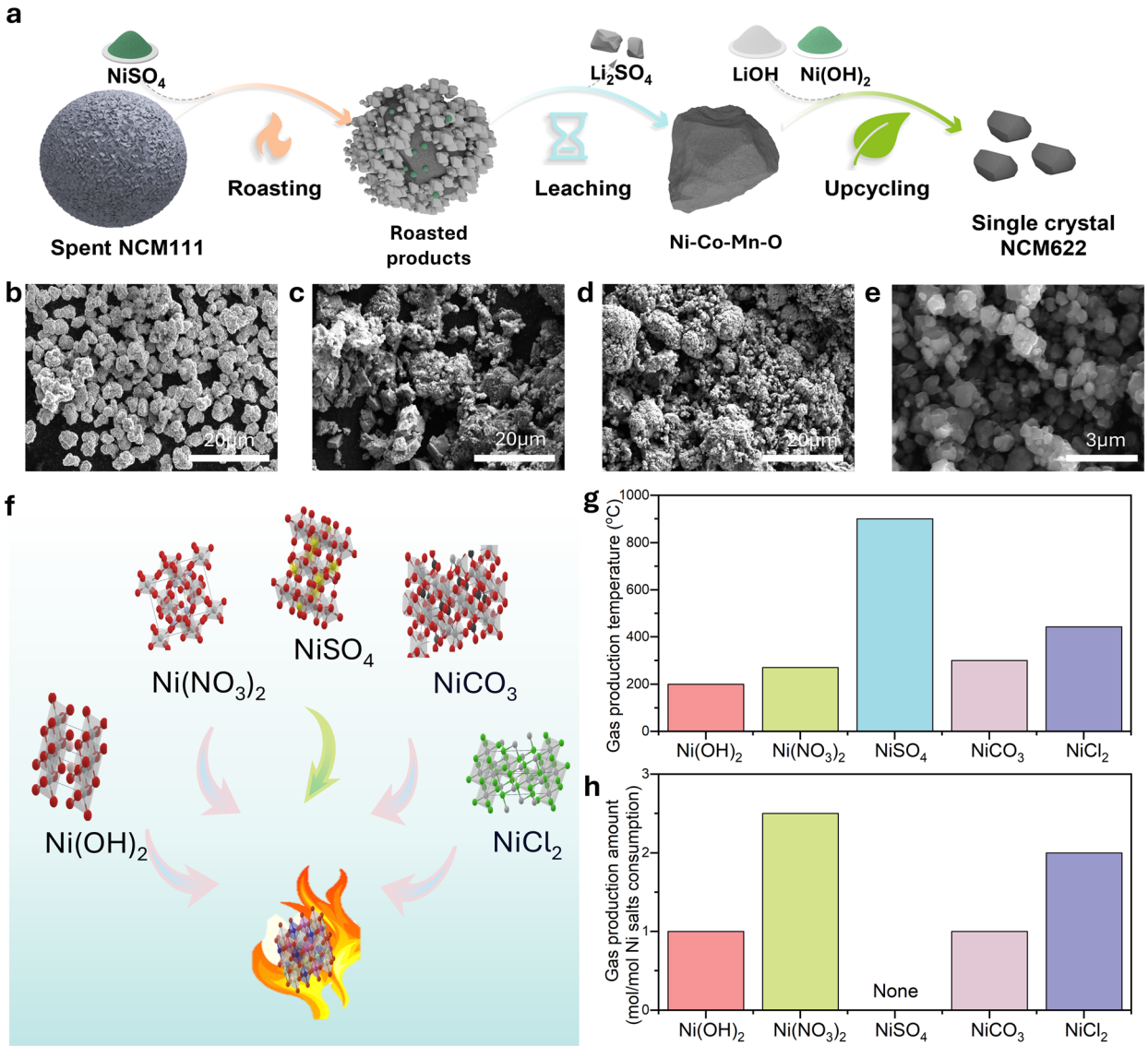

Fig. 1 Schematic illustration of the direct upcycling method. (a) The flowsheet for spent polycrystalline NCM111 through roasting, leaching, and upcycling into single crystal Ni-rich NCM. SEM images of (b) spent polycrystalline NCM111, (c) roasted products, (d) leached residue, and (e) single crystal NCM622 as an example. (f) Nickel source selection process considering the conversion mechanism of the selective recycling process. (g) Nickel source decomposition temperatures and (h) gas production amount during the roasting process in the air.

conformal NiO coating that protects the Ni–Co–Mn oxide core from structural breakdown (Fig. S3 and S4).[26] Upon subsequent sintering, the upcycled Ni-rich powder evolves into a single-crystalline morphology.

A key aspect of this upcycling process is the stability of the conversion agent at high temperatures, which is crucial for the successful extraction of Li from NCM during the thermally driven conversion stage.[24,26] We investigated the thermodynamic stability of potential conversion agents and their possible products across a temperature range from 298 to 1300 K. Among the commonly used nickel salts ($Ni(NO_3)_2$, $NiCO_3$, and $NiCl_2$) and $Ni(OH)_2$, only $NiSO_4$ remains thermally stable at typical lithium extraction temperatures (above 800 °C) without gas generation[24,27] (Fig. 1g, h and Fig. S5). Such unique reactivity and thermal stability justify our selection of $NiSO_4$ as the conversion agent for this process. Moreover, Ni occupies the octahedral center in the $NiSO_4$ crystal, aligning with the same lattice position in NCM materials. This suggests that the octahedral structure remains intact during the upcycling process, making this method well-suited for recovering and upgrading various NCM materials from the spent NCM111 cathode.

2.2 In-depth understanding of the upcycling process

To understand the structural conversions throughout the selective upcycling process, we characterized D-NCM111, roasted

Open Access Article. Published on 15 September 2025. Downloaded on 12/24/2025 10:16:25 PM.
This article is licensed under a Creative Commons Attribution-NonCommercial 3.0 Unported Licence.

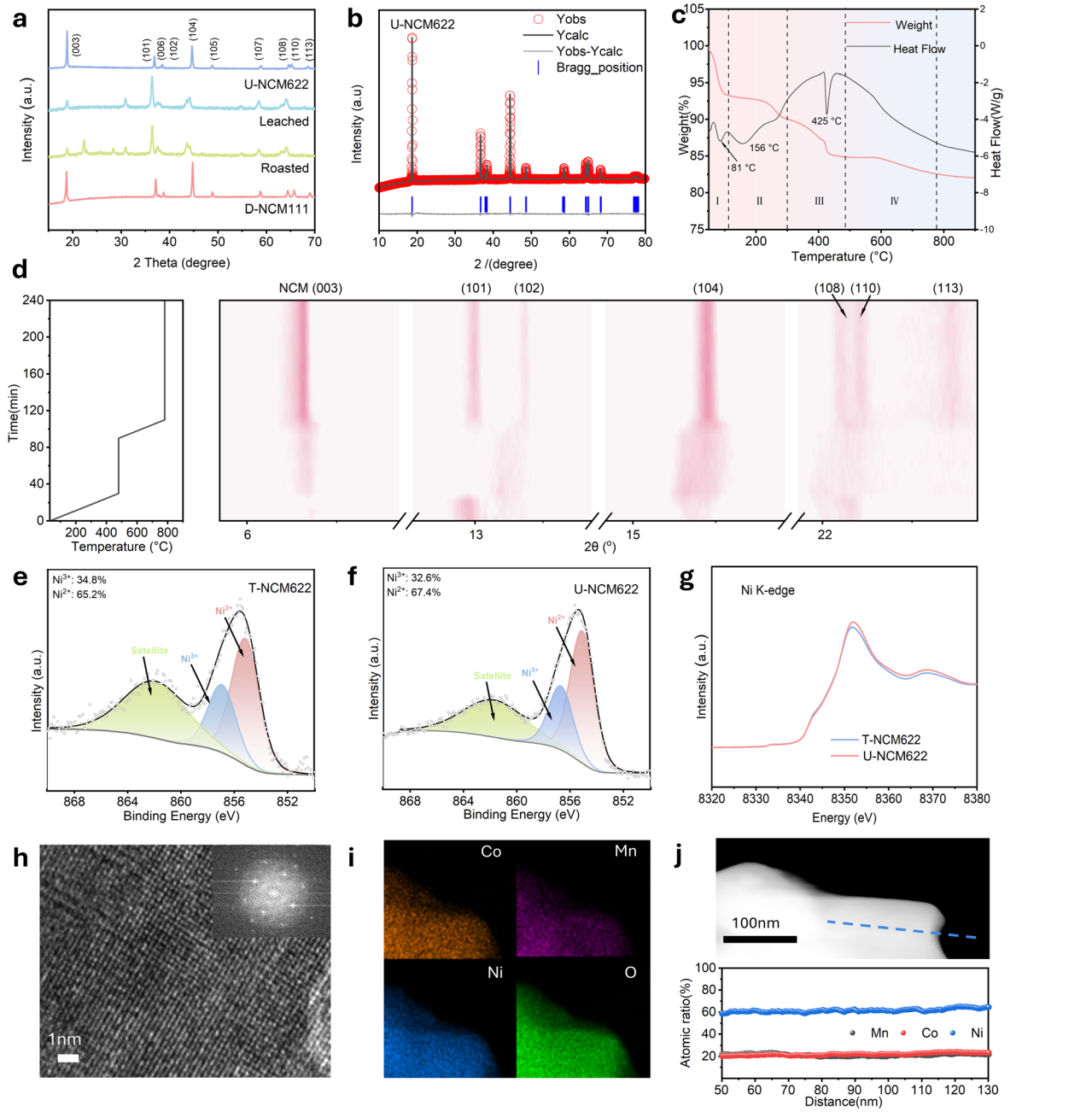

Fig. 2 Phase determination, thermodynamic understanding, and valence uniformity analyses of the selective upcycling process. (a) XRD patterns of delithiated NCM111, roasted products, leached residue, and U-NCM622. XRD refinement of (b) U-NCM622. TGA-DSC curves of (c) the leachate, LiOH, and $Ni(OH)_2$ mixture. Two-dimensional contour plot of the *in situ* XRD patterns recorded during the conversion of (d) the mixture of leachate, LiOH, and $Ni(OH)_2$ into an U-NCM622. XPS spectra of (e) T-NCM622 and (f) U-NCM622. (g) Calculated K-edge XAFS spectra of T-NCM622 and U-NCM622. (h) HRSTEM image of U-NCM622 with an inset image of the FFT pattern. (i) TEM-EDS mapping of Ni, Co, O, and Mn. (j) EDS linear scanning with inset elemental distribution intensity.

products, TMO residues, and upcycled NCM622 (U-NCM622) with X-ray diffraction (XRD) measurements (Fig. 2a). After calcination, D-NCM111 was converted by $NiSO_4{\cdot}6H_2O$ into Li_2SO_4 and TMO. A comparison of the XRD patterns of the roasted products and TMO residues revealed the absence of the Li_2SO_4 phase after the leaching. Coupled plasma mass spectrometry (ICP–MS) results further confirmed that lithium was completely extracted. The selective extraction efficiency for each element was calculated using eqn (1):

$$S_m = \frac{C_m}{\sum_i C_i} \times 100\% = \frac{m_{bi} - m_{ii}}{M_m \sum_i \frac{m_{bi} - m_{ii}}{M_i}} \times 100\% \quad (1)$$

© 2025 The Author(s). Published by the Royal Society of Chemistry

Open Access Article. Published on 15 September 2025. Downloaded on 12/24/2025 10:16:25 PM.
This article is licensed under a Creative Commons Attribution-NonCommercial 3.0 Unported Licence.

where C_m represents the concentration of target metal "m" in the leaching solution, C_i represents the concentration of metal "i" in the leaching solution, m_{bi} represents the mass of the target metal "m" in the calcined sample, m_{ii} represents the mass of metal "i" in the calcined sample, M_m represents the relative atomic mass of the target metal "m" and M_i represents the relative atomic mass of metal "i". Lithium exhibited the highest selectivity (97.88%), while the selectivity for transition metal elements (including Ni, Co, and Mn) was only 2.11% (Fig. S6). Thus, the selectivity for lithium was significantly superior to that of other metals. These results suggest that under the thermally driven conditions, $NiSO_4$ can be effectively used as an additive to promote the conversion of D-NCM111 into the TMO precursor, and a simple water-based leaching method can be employed to selectively extract and recover lithium from the roasted products.

Through the selective upcycling method described above, Ni-rich NCM single crystals with the desired composition were obtained, as confirmed by ICP-MS (Table S1). 10% lithium-deficient D-NCM 111 ($Li_{0.90}Ni_{0.33}Co_{0.33}Mn_{0.33}O_2$) was transformed into fully lithiated NCM primary particles ($Li_{1.04}Ni_{0.60}Co_{0.20}Mn_{0.20}O_2$ and $Li_{1.06}Ni_{0.80}Co_{0.10}Mn_{0.10}O_2$) of single crystal particles. To demonstrate the effectiveness of our selective upcycling method, Fig. 2b and Fig. S7, S8 show the XRD patterns of U-NCM622 and U-NCM811 under optimized synthesis conditions. All samples confirmed the standard pattern of a hexagonal α-$NaFeO_2$-type structure in the $R\bar{3}m$ space group, with no detectable phase impurities.[28,29] The peak positions of all upcycled samples and the pristine polycrystalline NCM samples (T-NCM 622 and T-NCM 811) matched very closely, indicating the successful construction of a pure high-nickel phase. Notably, the peak intensity ratio of $I_{(003)}/I_{(104)}$ in the single-crystal U-NCM622 samples was higher than 1.85, compared to 1.37 in the pristine polycrystalline T-NCM622 particles, indicating a highly ordered lattice structure and reduced Li/Ni mixing in the single crystals.[30,31] This was further evidenced by the Rietveld refinement of the XRD pattern of U-NCM622 (Fig. 2b). According to the Rietveld refinement results given in Table S2, the Li/Ni mixing in U-NCM622 was lower (3.76%) compared to 4.55% in T-NCM 622. This reduction is attributed to the highly ordered structure suppressing oxygen release, thus reducing oxygen loss and Ni^{2+} content in U-NCM622, consequently mitigating Li/Ni mixing in single crystal U-NCM622 particles.

To investigate the conversion mechanism of the selective upcycling process, we considered the relevant reactions and their associated Gibbs free energy as follows:

$$LiNi_{0.33}Co_{0.33}Mn_{0.33}O_2 + 2NiSO_2 = 0.5Li_2SO_4 + 0.5NiO + Ni_{0.33}Co_{0.33}Mn_{0.33}O_{1.5} \quad (2)$$
$$\Delta_r G_T{}^\theta = 30.90 - 0.05T, \quad (298 - 2000\,K)$$

$$0.3NiO + 0.6Ni_{0.33}Co_{0.33}Mn_{0.33}O_{1.5} + 0.1Ni(OH)_2 + LiOH + 0.05O_2 = LiNi_{0.6}Co_{0.2}Mn_{0.2}O_2 + 0.6H_2O \quad (3)$$
$$\Delta_r G_T{}^\theta = 175.15 - 0.19T, \quad (298 - 2000\,K)$$

$$0.3NiO + 0.6Ni_{0.33}Co_{0.33}Mn_{0.33}O_{1.5} + 1.1Ni(OH)_2 + 2LiOH + 0.65O_2 = 2LiNi_{0.8}Co_{0.1}Mn_{0.1}O_2 + 2.1H_2O \quad (4)$$
$$\Delta_r G_T{}^\theta = 204.24 - 0.23T, \quad (298 - 2000\,K)$$

Fig. S9 displays the relationship between ΔG and temperature for different reactions. As depicted, $NiSO_4$ can transform NCM111 into Li_2SO_4, NiO, and Ni–Co–Mn oxides at high temperatures (eqn (2)). At a theoretical reaction temperature of 618 K (345 °C), $\Delta_r G_T{}^\theta = 0$. When the calcination temperature reaches 823 K (550 °C), the $\Delta_r G_T{}^\theta$ for reaction (2) becomes negative, explaining why this transformation can complete at 550 °C. Since $NiSO_4$ decomposes only above 800 °C, it remains stable during thermally driven conversion at 550 °C, facilitating solid-phase reaction with NCM. Similarly, Li_2SO_4, which decomposes above 1000 °C, also remains stable throughout the roasting process. Consequently, the entire transformation process is environmentally benign, not producing or emitting SO_x.[24] In reactions (3) and (4), at high temperatures, Ni–Co–Mn oxides can react with a certain amount of $Ni(OH)_2$ and LiOH to be converted into NCM622 and NCM811, respectively. The theoretical reaction temperature for $\Delta_r G_T{}^\theta$ to reach 0 is 922 K (648 °C) for NCM622 and 888 K (615 °C) for NCM811. This indicates that NCM811 can be synthesized at a lower temperature than NCM622 under the experimental conditions. At calcination temperatures of 1053 K (780 °C) for NCM622 and 993 K (720 °C) for NCM811, $\Delta_r G_T{}^\theta$ for both reactions becomes negative, confirming why these reactions occur at 780 °C and 720 °C, respectively, as used in this study. Under optimal conditions, a similar methodology can be applied to synthesize both NCM622 and NCM811 with no apparent lithium salt residues on their surface (Fig. S10).

Thermogravimetric analysis and differential scanning calorimetry (TGA-DSC) analysis (Fig. S11) illustrate the evolution of each constituent during the roasting process. TGA-DSC analysis shows that $NiSO_4{\cdot}6H_2O$ undergoes gradual dehydration and continuous mass loss within the roasting temperature range. TGA-DSC analysis (Fig. 2c) further illustrates the evolution of the precursor constituent during the upcycling process of NCM622. Phase I involves surface H_2O loss. Phase II sees $LiOH{\cdot}H_2O$ losing H_2O to form LiOH and Ni$(OH)_2$ decomposing into NiO_x. In phase III, LiOH begins to melt, and in phase IV, the Ni–Co–Mn oxides react with NiO_x in the LiOH solution. According to the upcycling process protocol, the temperature is maintained at 480 °C for 6 hours, allowing the LiOH solution to form a uniform mixture with Ni–Co–Mn oxides and the decomposed $Ni(OH)_2$ precursor. Prolonged high-temperature sintering results in fully lithiated single-crystal U-NCM 622.

In situ XRD experiments provided further insights into the structural evolution of the mixture of the leachate, LiOH, and $Ni(OH)_2$ during the upcycling process (Fig. 2d). The whole process can be divided into two steps in terms of phase transformation. As the temperature increases to 480 °C, the intensity of the leachate and LiOH gradually decreases as LiOH starts to react with Ni–Co–Mn oxides. As the temperature increases to 780 °C, the (003) and (104) peaks associated with

Open Access Article. Published on 15 September 2025. Downloaded on 12/24/2025 10:16:25 PM.
This article is licensed under a Creative Commons Attribution-NonCommercial 3.0 Unported Licence.

the layered structure gradually increase in intensity. The initially merged (103) and (110) peaks in the degraded NCM622 become separated, which also indicates the re-assembly of the layered structure.[32] These findings confirm the formation of layered structures during the upcycling process, supporting previous *ex situ* XRD and TGA results.

X-ray photoelectron spectroscopy (XPS) analysis was performed on T-NCM622 and U-NCM622 to examine the valence states of the transition metals. The Ni 2p3/2 spectra, as illustrated in Fig. 2e and f, reveal a similar Ni^{3+}/Ni^{2+} ratio between T-NCM622 and U-NCM 622, indicating a consistent average valence of Ni in both samples. These XPS findings align with data from the Ni K-edge in the X-ray absorption fine structure (XAFS) spectrum for both samples (Fig. 2g). It is shown that the valence ratio, bonding state, and coordination environment within the structure of U-NCM 622 are comparable to those observed in T-NCM622. Based on the XPS S 2p spectra of upcycled U-NCM622 and T-NCM622 (Fig. S12), no S-related peaks were detected in either upcycled U-NCM622 or T-NCM622, indicating the absence of SO_4^{2-} species on the upcycled cathode surface.

To gain further insight into the microstructural characteristics of U-NCM622, a focused ion beam (FIB) cross-section was used to create a cross-sectional view. Fig. S13 shows that U-NCM622 lacks cavities, cracks, or visible grain boundaries. The high-resolution high-angle annular dark-field (HAADF)-STEM images, coupled with a fast Fourier transform (FFT) pattern, confirm the homogeneous α-$NaFeO_2$-type layered structures (Fig. 2h). Energy-dispersive X-ray spectroscopy (EDS) mapping illustrates a uniform local distribution of Ni, Mn, and Co at the nanometer scale (Fig. 2i). The linear scanning substantiates the atomic ratio of Ni, Mn, and Co as 6 : 2 : 2 with high uniformity in the examined grain (Fig. 2j).

2.3 Electrochemical performance of upcycled NCMs

The electrochemical performance of U-NCM622 was examined using coin cells with a cathode mass loading of ~5 mg cm^{-2} and Gen2 (1.2 M $LiPF_6$ in EC/EMC = 3 : 7) electrolyte and compared with that of T-NCM622. As shown in Fig. 3a and b, at C/3, U-NCM622 exhibited an initial capacity of 176 mAh g^{-1} with a retention of 92.8% after 100 cycles. This performance is comparable to that of pristine T-NCM622, which exhibited a capacity retention of 92.4%. This signifies that U-NCM622 can achieve similar cycling stability to pristine T-NCM622. Rate capability testing further demonstrated that U-NCM622 exhibited comparable electrochemical performances to T-NCM622 across all tested rates (Fig. 3c), confirming the effectiveness of our upcycling method. Full-cell tests were also conducted, pairing these cathodes (with a mass loading of 14 mg cm^{-2}) with a commercial graphite anode (Fig. 3d) at a N/P ratio of 1.1 : 1. In this setup, U-NCM622 showed an initial capacity of 153 mAh g^{-1} at 1C and maintained the capacity of 130 mAh g^{-1} after 100 cycles, comparable to that of pristine T-NCM622 under the same conditions. Additionally, Fig. 3e and f show that while pristine T-NCM811 (commercial polycrystalline NCM811) delivers higher initial discharge capacity than U-NCM811, which may be due to its smaller primary particle size and larger specific surface area, T-NCM811 exhibits lower rate performance compared to U-NCM811, which can be attributed to increased grain boundary resistance and more severe side reactions under high current conditions.[28] U-NCM811 demonstrated good electrochemical performance, with a capacity retention of 88.9% after 100 cycles, on par with T-NCM811 in the control experiment. These results further validate the success of the selective upcycling process in producing cathode materials with electrochemical performance equivalent to pristine materials.

2.4 Feasibility investigation

In practical scenarios, spent NCM111 black mass ("NCM111-BM") is obtained from end-of-life cells. To demonstrate the versatility of our selective upcycling process with a more practical feedstock, we applied it to NCM111-BM for evaluation.[7] The overall procedure remained the same as the process for upcycling D-NCM111. NCM111-BM consists of a degraded cathode active material, a residual PVDF binder, conductive carbon, and electrolyte salt after pre-procesing,[33] as shown in the backscattering mode SEM image in Fig. 4a. After roasting and leaching steps, the particle surfaces appear clean (Fig. S14), confirming the effective removal of the carbon black, PVDF, and salt residues. After upcycling, the U-NCM622-BM shows a clean particle surface and the formation of single-crystal particles (Fig. 4b), demonstrating that the process simultaneously removes surface residues and achieves effective structural regeneration. This was further corroborated by XPS analysis of F1s, as shown in Fig. 4c, d and Fig. S15, indicating that the PVDF binder, conductive carbon, and salt residues could be eliminated after the roasting and leaching steps. XRD results (Fig. S16) reveal that the (003), (108), and (110) peaks of U-NCM622-BM closely match those of T-NCM622, indicating the success of the upcycling process. Half-cells composed of U-NCM622-BM as the cathode demonstrated an initial coulombic efficiency (ICE) of 86% with a discharge capacity of 173 mAh g^{-1}, close to that of T-NCM622. Long-term cycling data for these half-cells showed a commendable 87.8% capacity retention after 100 cycles (Fig. 4e and f), underscoring the high quality of the U-NCM622 cathode materials using real cathode black mass. We further validated our process by scaling up to a 10 g batch of U-NCM622 (U-NCM622-BM-10 g) prepared using the same pelletized sintering protocol as in the small-batch synthesis. The long-term cycling performance of these half-cells demonstrated the capacity retention of 87.3% after 100 cycles (Fig. S17), highlighting the scalability of the U-NCM622 cathode materials and the versatility of our selective upcycling process for processing real cathode black mass in practical applications. This upcycling strategy, although demonstrated on NCM111, is in principle extendable to other layered oxide cathodes—including $LiNi_xCo_yAl_{1-x-y}O_2$ (NCA) and Ni-rich NCMs—through appropriate adjustment of precursor ratios and sintering conditions.

© 2025 The Author(s). Published by the Royal Society of Chemistry

Open Access Article. Published on 15 September 2025. Downloaded on 12/24/2025 10:16:25 PM.
This article is licensed under a Creative Commons Attribution-NonCommercial 3.0 Unported Licence.

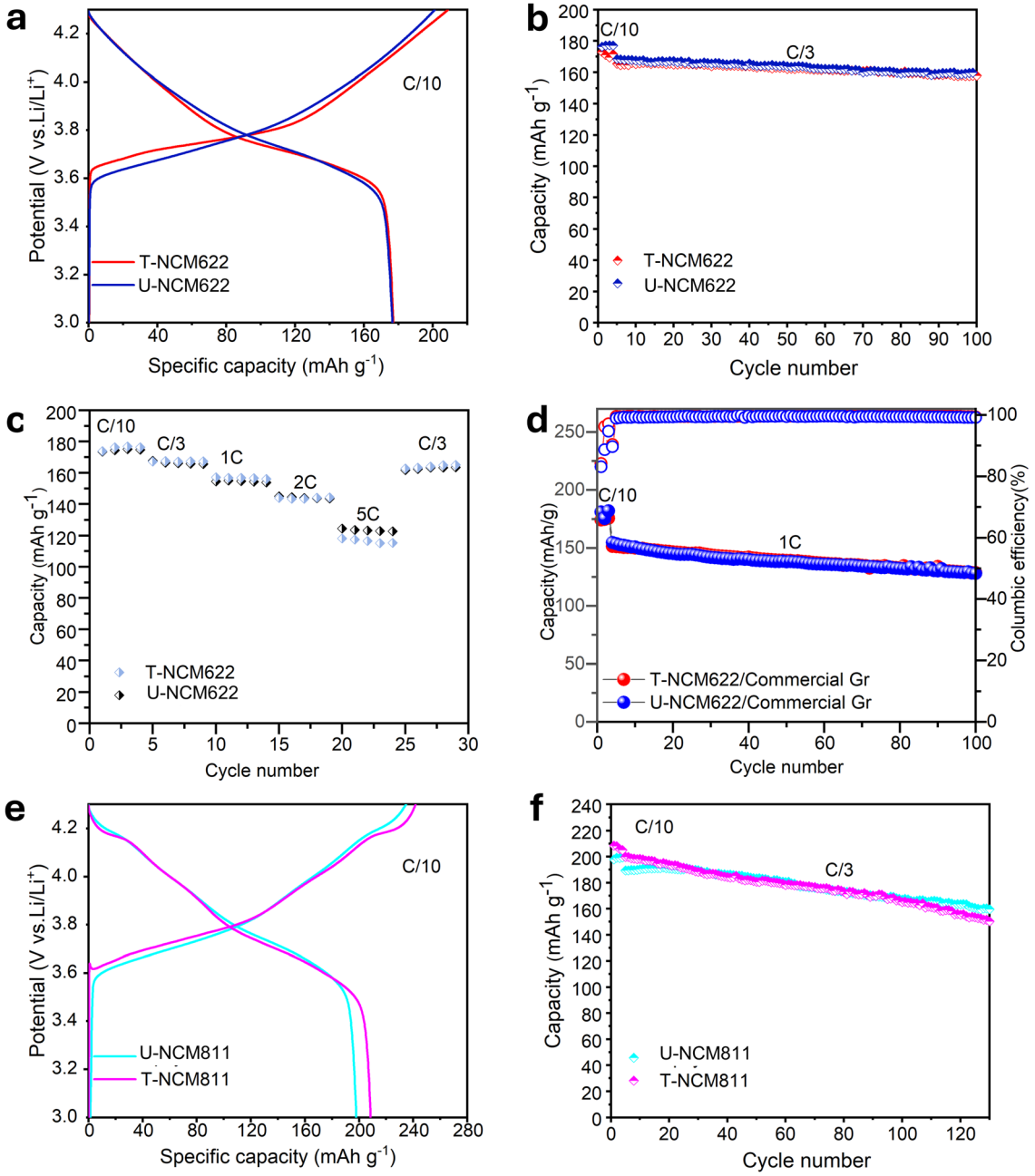

Fig. 3 Electrochemical performance evaluation of upcycled materials. (a) First cycle voltage profiles, (b) cycling stability, and (c) rate performance of U-NCM622 compared with those of pristine T-NCM622. (d) Full cell cycling stability of the U-NCM622 sample compared with that of pristine T-NCM622 at 1C. (e) First cycle voltage profiles and (f) cycling stability of U-NCM 811 compared with those of pristine T-NCM811.

2.5 Economic and environmental analysis

We further adopted the EverBatt model[34] to evaluate different recycling processes to assess the environmental and economic benefits, demonstrating that selective upcycling could be both cost-effective and sustainable. Further details on the methodologies used are available in the SI. Modifications were made to the EverBatt model's flow charts to adapt them to the revised process designs. As illustrated in Fig. S18, the selective upcycling process involves discharging, dismantling, and crushing the battery.[35] This is followed by a physical separation method to isolate metals, plastics, and cathode materials. These materials are then subjected to roasting and upcycling to produce U-NCM622 cathode powders. Comparative flow charts for selective upcycling, pyrometallurgical, hydrometallurgical, and cathode powder production processes are displayed in Fig. S18, S19, S20 and S21, respectively.

In terms of cumulative energy consumption (Fig. S22a), the EverBatt modeling results project that manufacturing accounts for the highest energy input, primarily due to the upstream

Open Access Article. Published on 15 September 2025. Downloaded on 12/24/2025 10:16:25 PM.
This article is licensed under a Creative Commons Attribution-NonCommercial 3.0 Unported Licence.

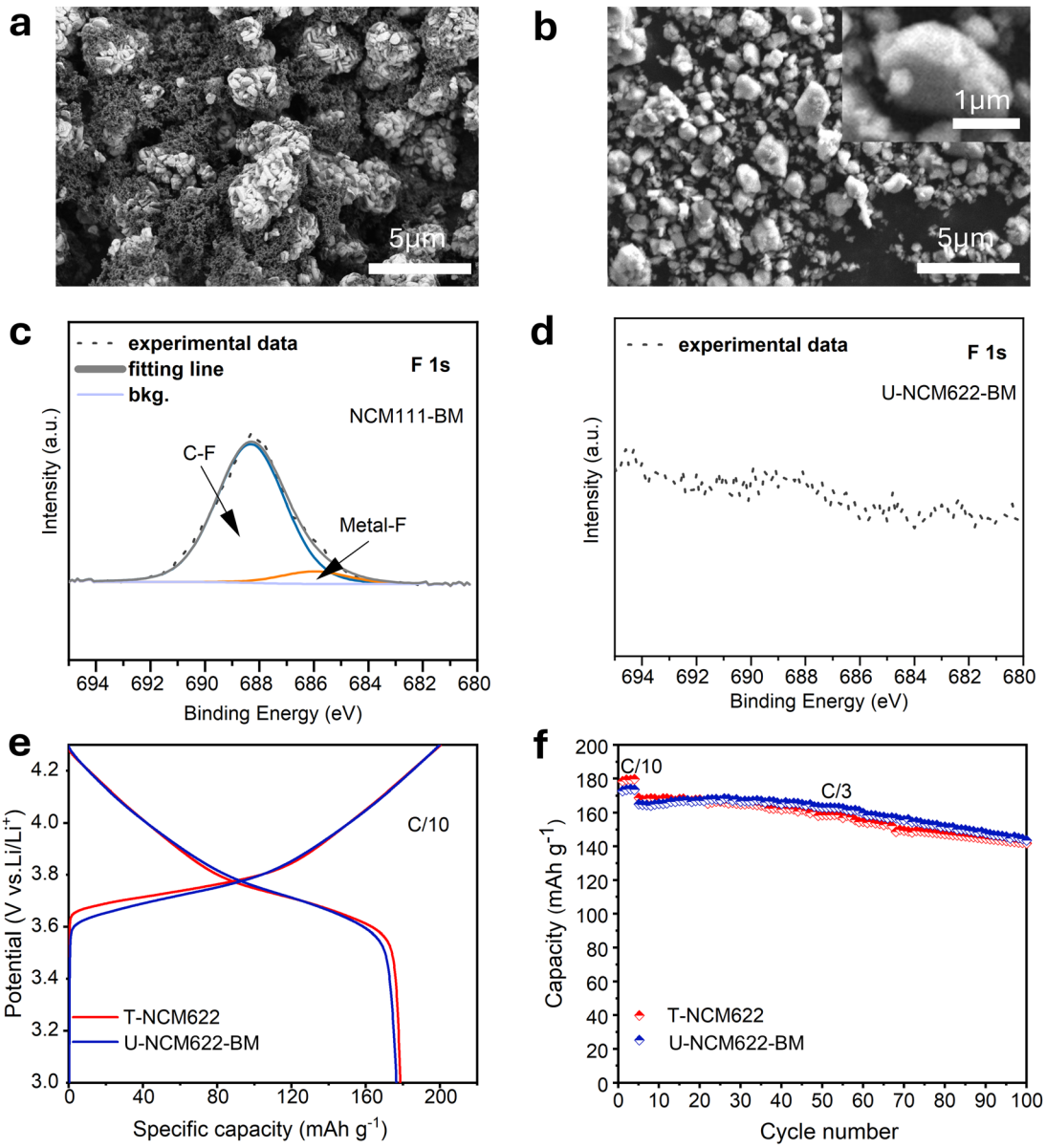

Fig. 4 Feasibility demonstration. SEM images of (a) spent NCM111 black mass and (b) upcycled NCM622 (U-NCM622-BM) using NCM111 cathode black mass from an EV battery as raw materials. XPS data of fluorine for (c) spent NCM111 black mass and (d) U-NCM622-BM to indicate the removal of the binder from the recovered cathode through a selective upcycling process. (e) First cycle voltage profile and (f) cycling stability for U-NCM622-BM, compared with those of T-NCM622.

production of chemical reagents required in conventional cathode production processes. Among the methods evaluated, pyrometallurgy exhibited higher energy consumption than hydrometallurgy, owing to the elevated temperatures required during the smelting stage. These trends underscore that the dominant contributors to energy consumption are raw material inputs and high-energy equipment. In contrast, the selective upcycling process—revised and implemented within the EverBatt model—relies only on minimal reagents, namely $NiSO_4$ and $Ni(OH)_2$, whose quantities are determined by the lithium loss from the spent cathode and the nickel content of the target product. Therefore, due to reduced chemical usage, the absence of high-temperature operations, and simplified processing, selective upcycling achieved a cumulative energy consumption of just 43.4 MJ per kg of spent cathode material —approximately 15% of that required for hydrometallurgical recycling. Additionally, selective upcycling circumvents the usage of energy-intensive equipment employed in the pyrometallurgical recycling process.

When evaluating greenhouse gas (GHG) emissions (Fig. S22b), both pyrometallurgical and hydrometallurgical routes exhibited significantly higher emissions compared to selective upcycling. The majority of GHG emissions in pyrometallurgy stem from the smelting stage, while those in hydrome-

© 2025 The Author(s). Published by the Royal Society of Chemistry

Open Access Article. Published on 15 September 2025. Downloaded on 12/24/2025 10:16:25 PM.
This article is licensed under a Creative Commons Attribution-NonCommercial 3.0 Unported Licence.

tallurgy originate mainly from the upstream chemical manufacturing. Notably, the selective upcycling process released only 3.75 kg of GHG per 1 kg of spent cathode recycled, markedly lower than those from pyrometallurgy (21.35 kg) and hydrometallurgy (19.8 kg).

The spider diagram offers a detailed comparison of these recycling methods, highlighting the clear benefits of selective upcycling in terms of energy use, GHG emissions, chemical waste, simplicity of operations, and revenue, as shown in Fig. 5a–d and Fig. S22. Technically, this selective upcycling process represents a major step, bridging the gap between laboratory-scale recycling and its industrial implementation. Historical data suggest that while regenerated cathode materials were once top-grade, they now fail to meet modern standards, necessitating an upgrade.[9] This process revitalizes outdated cathode materials, transforming them into cutting-edge materials with superior capacity and energy density. This scalable application significantly enhances the electrochemical performance of spent cathode active materials.[11,36] By upgrading and recycling cathode materials, there are considerable gains in value, adaptability in development, and support for the sustainable development of the lithium-ion battery industry.

3. Conclusion

In summary, we have successfully demonstrated an effective strategy for the thermally driven selective upcycling process of spent cathodes. Our method involves the selective extraction of lithium from spent polycrystalline NCM111 and the conversion of residues into single-crystal NCM622 particles with the desired Ni content. The process employs $NiSO_4$ for lithium extraction while maintaining sulfur as SO_4^{2-} throughout the process to prevent contamination. This facile process achieves the desired composition and high phase purity in the upcycled single-crystal particles, resulting in comparable rate performance and cycling stability compared to the original polycrystalline cathodes. Life-cycle analysis demonstrates that this method significantly reduces energy consumption and greenhouse gas emissions, offering superior economic and environmental benefits over traditional hydrometallurgical, pyrometallurgical, and cathode production techniques. This study paves a path for the efficient upcycling of spent LIB materials, accommodating the diverse chemistries used in current NCM cells, and contributes to the development of the next generation of selective recovery and upcycling strategies for sustainable energy storage in lithium-ion batteries.

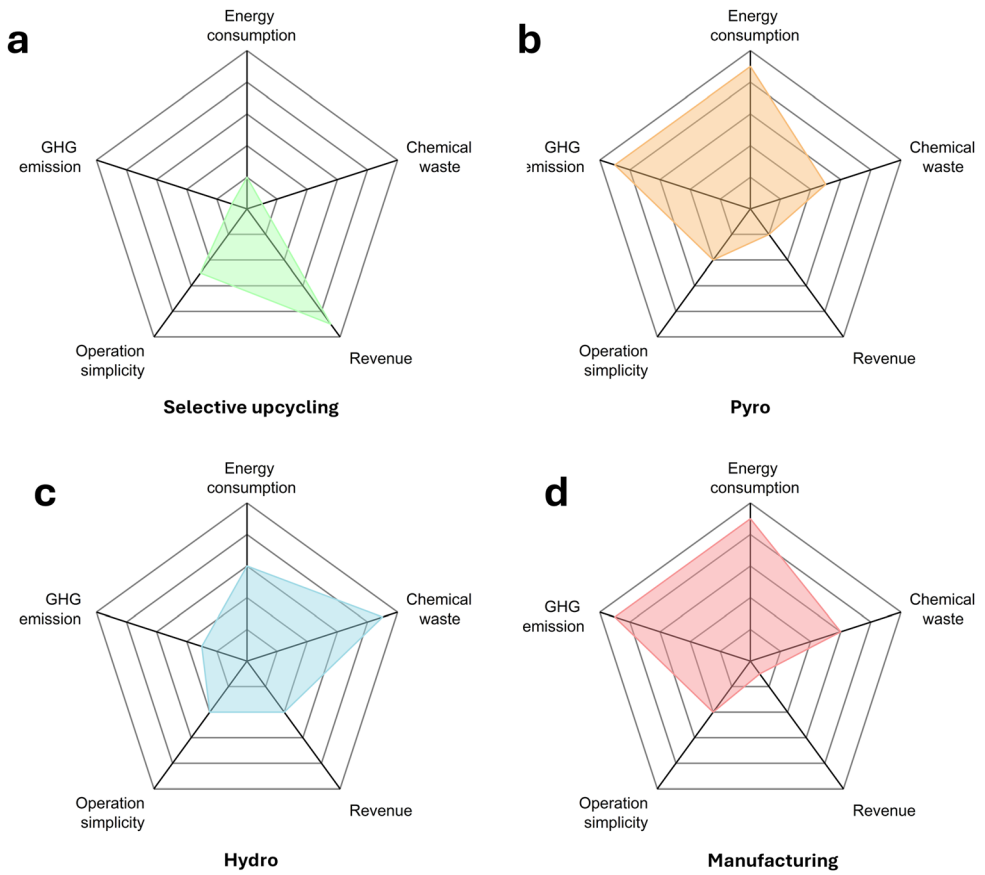

Fig. 5 Economic and environmental analysis. Schematic of this work ("selective upcycling"), pyrometallurgical ("Pyro"), and hydrometallurgical ("Hydro") methods, as well as cathode production ("Manufacturing") from virgin materials mining. Spider charts comparing various features of (a) this work, (b) Pyro, (c) Hydro, and (d) cathode production methods.

© 2025 The Author(s). Published by the Royal Society of Chemistry

Open Access Article. Published on 15 September 2025. Downloaded on 12/24/2025 10:16:25 PM.
This article is licensed under a Creative Commons Attribution-NonCommercial 3.0 Unported Licence.

4. Methods

4.1 Chemically delithiated NCM111 and electrochemically degraded NCM111

Materials Engineering Research Facility (MERF) from Argonne National Laboratory produced chemically delithiated NCM111, labeled as "D-NCM111", with about 10% lithium removed. The pristine NCM111 material, supplied by Toda America Inc., was reacted with an aqueous potassium persulfate solution to extract lithium. It was then washed with water and acetonitrile before being dried under vacuum at room temperature. This 1 kg batch of D-NCM111 was used as the starting material for our additive screening experiments.

End-of-life 20 Ah prismatic NCM111 cells were provided by American HONDA Motor Company. These cells were manually disassembled in a fume hood, and the long cathode strips were cut into pieces approximately 5 × 5 inches in size. After disassembly, the cathode strips were stored in the fume hood for two days, and then dried overnight in a vacuum oven at 80 °C. Degraded NCM 111 was obtained by scratching these cathode strips with blade.

4.2 Selective upcycling

D-NCM111 was ground and mixed with $NiSO_4{\cdot}6H_2O$, and then roasted in a muffle furnace at a heating rate of 5 °C min^{-1} at 550 °C for 60 min. The roasted product was ground and leached with deionized water at a solid–liquid ratio of 150 g L^{-1} for 90 min at room temperature. The insoluble leached residue was filtered and dried overnight at 80 °C in a vacuum oven. 5 g of leached residues and certain amounts of Ni precursor (calculated based on the end product) were mixed in 10 ml of ethanol by planetary ball milling (XIAMEN TMAX) at 600 rpm. The mixture was collected after drying in a vacuum oven at 80 °C for 2 hours. 1 g of ball milled mixture was pelleted with a 1.07x molar ratio (based on the stoichiometry in the final product, $Li_{1.1}Ni_xCo_yMn_zO_2$, for compensating the Li loss during sintering) of LiOH.

For sintering, the pellet was held at 480 °C for 6 h with a ramping rate of 5 °C min^{-1} and then held at 780 °C for 12 h with a ramping rate of 5 °C min^{-1} under a pure oxygen atmosphere. The optimal conditions for upcycling NCM 622 are sintering the pellet at 780 °C for 12 h. For black mass upcycling, the same process is performed. The optimal conditions for upcycling NCM 811 are sintering the pellet at 720 °C for 12 h.

4.3 Materials characterization

The crystal structure was determined by X-ray powder diffraction (XRD) using Cu Kα radiation (λ = 1.5406 Å) with a Bruker D2 Phaser, and Rietveld refinement of the XRD results was performed using the General Structure Analysis System (GSAS) software with the FullProf_Suite interface. The thermogravimetric analysis (TGA) and differential scanning calorimetry (DSC) curves of the upcycling process were collected in alumina pans using Instruments™ Discovery SDT 650™ simultaneous DSC/TGA in UC San Diego Materials Research Science and Engineering Center (UCSD MRSEC). The chemical composition of various cathode powders was evaluated using ICP–MS with the Thermo Scientific iCAP RQ model. Surface composition analysis was conducted through X-ray photoelectron spectroscopy (XPS) with data collected on the PHI 5000 VersaProbe II system (Physical Electronics), utilizing Al Kα radiation at 1486.6 eV. The surface and bulk morphology of the different NCM cathode particles were examined using a scanning electron microscope (SEM), specifically FEI XL30. The particle cross-section experiment was performed using an FEI Scios DualBeam FIB/SEM. High-resolution transmission electron microscopy (HRTEM) was performed on a Thermo Fisher Talos 200X TEM operating at 200 kV with a CETA Camera. STEM was conducted on primary particles in high-angle annular dark-field imaging (HAADF) mode using the same instrument. Ni K-edge XAFS spectra were collected at the Stanford Synchrotron Radiation Lightsource (SSRL), at the Molecular Environmental and Interface Science beamline (11–2) at 298 K using a cryogenically cooled double-crystal Si (220) monochromator (U = 0°).

4.4 Electrochemical characterization

The electrochemical performance of all samples was assessed using coin cells in a half-cell configuration with a cathode mass loading of approximately 5 mg cm^{-2}. To prepare the electrode slurries, the pristine, upcycled NCM cathode material was mixed with a conductive agent (Super P65) and a polyvinylidene fluoride (PVDF) binder in a mass ratio of 8 : 1 : 1 in *N*-methyl-2-pyrrolidone (NMP) solvent. The slurries were then applied to aluminum foil using a doctor blade and dried at 120 °C for 12 hours in a vacuum oven. The dry laminate was cut into disc shapes and calendared. Coin cells were assembled inside a glovebox, using a 1.1 mm thick Li metal disc as the counter electrode, Gen2 (1.2 M $LiPF_6$ in EC/EMC = 3 : 7) as the electrolyte, and a tri-layer membrane (Celgard 2320) as the separator. Galvanostatic charge–discharge tests were performed with a Neware battery cycler within the potential range of 3.0–4.3 V, including 4 activation cycles at a rate of C/10, followed by 100 cycles at a rate of C/3.

For making full-cells, the cathode composition is cathode : PVDF (Kynar HSV 1800) : carbon black (Super-P) at a 90 : 5 : 5 wt% ratio. The areal capacity is 2.7 mAh cm^{-2}. The anode composition is graphite (Carnad Ltd) : (Kynar HSV 1800) : carbon black (Super-P) at a 90 : 5 : 5 wt% ratio. The anode areal capacity is 3 mAh cm^{-2}. The slurries of cathode and anode materials were cast on aluminum and copper foils, respectively. Both cathode and anode electrodes were transferred into a vacuum oven for drying overnight at 120 °C and 80 °C, respectively. CR-2032 type coin cells were assembled with the prepared cathodes and anodes (N/P ratio = 1.1) with a trilayer membrane (Celgard 2325) as the separator soaked in 70 μL of electrolyte. Galvanostatic charge–discharge was tested using a Neware battery cycler in the potential range of 2.8 V–4.2 V at room temperatures with 4 activation cycles at the rate of C/10 followed by long cycles at a constant rate of 1C.

© 2025 The Author(s). Published by the Royal Society of Chemistry

Open Access Article. Published on 15 September 2025. Downloaded on 12/24/2025 10:16:25 PM. This article is licensed under a Creative Commons Attribution-NonCommercial 3.0 Unported Licence.

4.5 Economic and environmental analyses

To analyze the differences in the techno-economic aspects and life cycle evaluations between the traditional cathode production and selective upcycling methods, we used the EverBatt model. Developed at Argonne National Laboratory, EverBatt is a closed-loop battery recycling model. It assumes that all recycling methods can process an annual capacity of 10 000 metric tons of battery cells in the United States.[34]

Conflicts of interest

The authors declare no conflict of interest.

Data availability

The data supporting this article have been included as part of the SI. Supplementary information is available, including XRD, SEM, XPS, TG-DSC, FIB, cycling performance, voltage profiles, ICP data, and EverBatt model details. See DOI: https://doi.org/10.1039/d5eb00128e.

Acknowledgements

We gratefully acknowledge support from the California Energy Commission (Grant No. EPC-23-023). Use of the Stanford Synchrotron Radiation Light source, SLAC National Accelerator Laboratory, is supported by the US Department of Energy, Office of Science, Office of Basic Energy Sciences, under Proposal No. S-XV-ST-5823. The authors also acknowledge the support from American Honda Manufacturing for donating spent EV batteries. We also thank Dr Christos D. Malliakas from Northwestern University for assistance with *in situ* XRD experiments.

References

1 G. Zhao and G. Zhao, *Market Development of Reuse and Recycling of Power Batteries*, 2017.
2 B. Huang, Z. F. Pan, X. Y. Su and L. An, *J. Power Sources*, 2018, **399**, 274–286.
3 L. Azhari, S. Bong, X. T. Ma and Y. Wang, *Matter*, 2020, **3**, 1845–1861.
4 X. Yu, W. Li, V. Gupta, H. Gao, D. Tran, S. Sarwar and Z. Chen, *Glob. Chall.*, 2022, **6**, 2200099.
5 P. Xu, D. H. S. Tan, B. Jiao, H. Gao, X. Yu and Z. Chen, *Adv. Funct. Mater.*, 2023, **33**, 2213168.
6 T. W. Zhang, J. Dao, J. S. Wang, Y. Z. Guo, R. D. Wan, C. P. Li, X. Zhou and Z. F. Zhang, *Front. Environ. Sci. Eng.*, 2024, **18**, 25.
7 V. Gupta, M. Appleberry, W. Li and Z. Chen, *Next Energy*, 2024, **2**, 100091.
8 H. Gao, D. Tran and Z. Chen, *Curr. Opin. Electrochem.*, 2022, **31**, 100875.
9 X. Xiao, L. Wang, Y. Wu, Y. Song, Z. Chen and X. He, *Energy Environ. Sci.*, 2023, **16**, 2856–2868.
10 O. Velazquez-Martinez, J. Valio, A. Santasalo-Aarnio, M. Reuter and R. Serna-Guerrero, *Batteries*, 2019, **5**, 68.
11 P. Xu, Q. Dai, H. Gao, H. Liu, M. Zhang, M. Li, Y. Chen, K. An, Y. S. Meng and P. Liu, *Joule*, 2020, **4**, 2609–2626.
12 Y. Shi, G. Chen and Z. Chen, *Green Chem.*, 2018, **20**, 851–862.
13 X. Yu, S. Yu, J. Lin, V. Gupta, H. Gao, W. Li, M. Appleberry, P. Liu and Z. Chen, *Adv. Mater.*, 2024, **36**, 2408463.
14 J. Ma, J. Wang, K. Jia, Z. Liang, G. Ji, H. Ji, Y. Zhu, W. Chen, H.-M. Cheng and G. Zhou, *Nat. Commun.*, 2024, **15**, 1046.
15 H. Gao, D. Tran and Z. Chen, *Curr. Opin. Electrochem.*, 2022, **31**, 100875.
16 T. Raj, K. Chandrasekhar, A. N. Kumar, P. Sharma, A. Pandey, M. Jang, B. H. Jeon, S. Varjani and S. H. Kim, *J. Hazard. Mater.*, 2022, **429**, 128312.
17 X. Xiao, L. Wang, Y. Wu, Y. Song, Z. Chen and X. He, *Energy Environ. Sci.*, 2023, **16**, 2856–2868.
18 J. Zhou, C. Xing, J. Huang, Y. Zhang, G. Li, L. Chen, S. Tao, Z. Yang, G. Wang and L. Fei, *Adv. Energy Mater.*, 2024, **14**, 2302761.
19 Y. Li, J. He, L. Luo, X. Li, Z. Chen, Y. Zhang, L. Deng, P. Dong, S. Yang, K. Wu, D. Wang, Y. Zhang and J. Duan, *ACS Appl. Energy Mater.*, 2022, **5**, 6302–6312.
20 X. T. Ma, J. H. Hou, P. Vanaphuti, Z. Y. Yao, J. Z. Fu, L. Azhari, Y. T. Liu and Y. Wang, *Chem*, 2022, **8**, 1944–1955.
21 G. Qian, Z. Li, Y. Wang, X. Xie, Y. He, J. Li, Y. Zhu, S. Xie, Z. Cheng, H. Che, Y. Shen, L. Chen, X. Huang, P. Pianetta, Z. F. Ma, Y. Liu and L. Li, *Cell Rep. Phys. Sci.*, 2022, **3**, 100741.
22 T. Wang, H. M. Luo, J. T. Fan, B. P. Thapaliya, Y. C. Bai, I. Belharouak and S. Dai, *iScience*, 2022, **25**, 103801.
23 H. Gao, Q. Yan, D. Tran, X. Yu, H. Liu, M. Li, W. Li, J. Wu, W. Tang, V. Gupta, J. Luo and Z. Chen, *ACS Energy Lett.*, 2023, **8**, 4136–4144.
24 J. Lin, C. Cui, X. Zhang, E. Fan, R. Chen, F. Wu and L. Li, *J. Hazard. Mater.*, 2022, **424**, 127757.
25 Z. Huang, W. Xu, Z. Zhao, D. Liu, L. He and X. Liu, *Chem. Eng. J.*, 2023, **467**, 143247.
26 J. Lin, L. Li, E. Fan, C. Liu, X. Zhang, H. Cao, Z. Sun and R. Chen, *ACS Appl. Mater. Interfaces*, 2020, **12**, 18482–18489.
27 M. K. King and M. K. Mahapatra, *Int. J. Thermophys.*, 2022, **43**, 32.
28 H. Gao, Q. Yan, D. Tran, X. Yu, H. Liu, M. Li, W. Li, J. Wu, W. Tang and V. Gupta, *ACS Energy Lett.*, 2023, **8**, 4136–4144.
29 Y. Shi, M. Zhang, Y. S. Meng and Z. Chen, *Adv. Energy Mater.*, 2019, **9**, 1900454.
30 N. V. Kosova, E. T. Devyatkina and V. V. Kaichev, *J. Power Sources*, 2007, **174**, 965–969.
31 X. Zhang, W. J. Jiang, A. Mauger, L. Qi, F. Gendron and C. M. Julien, *J. Power Sources*, 2010, **195**, 1292–1301.
32 G. Qian, Z. Li, Y. Wang, X. Xie, Y. He, J. Li, Y. Zhu, S. Xie, Z. Cheng, H. Che, Y. Shen, L. Chen, X. Huang, P. Pianetta, Z.-F. Ma, Y. Liu and L. Li, *Cell Rep. Phys. Sci.*, 2022, **3**, 100741.

© 2025 The Author(s). Published by the Royal Society of Chemistry

Open Access Article. Published on 15 September 2025. Downloaded on 12/24/2025 10:16:25 PM.
This article is licensed under a Creative Commons Attribution-NonCommercial 3.0 Unported Licence.

33 V. Gupta, X. Yu, H. Gao, C. Brooks, W. Li and Z. Chen, *Adv. Energy Mater.*, 2023, **13**, 2203093.
34 Q. Dai, J. Spangenberger, S. Ahmed, L. Gaines, J. C. Kelly and M. Wang, *EverBatt: A closed-loop battery recycling cost and environmental impacts model*, Argonne National Lab. (ANL), Argonne, IL (United States), 2019.
35 P. Xu, D. H. S. Tan, H. Gao, S. Rose and Z. Chen, in *Encyclopedia of Energy Storage*, ed. L. F. Cabeza, Elsevier, Oxford, 2022, pp. 98–107.
36 X. Yu, S. Yu, Z. Yang, H. Gao, P. Xu, G. Cai, S. Rose, C. Brooks, P. Liu and Z. Chen, *Energy Storage Mater.*, 2022, **51**, 54–62.

© 2025 The Author(s). Published by the Royal Society of Chemistry